processes

MDPI

Article

A Computational Acceleration Method for Three-Dimensional Condensed-Phase Detonation

Shuxia Jiang [1,2], Yaoxiang Wang [3], Guixue Qi [1,2], Song Peng [1,2], Qikui Yu [1,2], Jixi Zhang [1,2], Wencai Jiang [1,2] and Min Xiao [3,*]

[1] SINOPEC Key Laboratory of Development Technology of Sour Natural Gas Fields, Puyang 457001, China
[2] Exploration and Development Research Institute, Zhongyuan Oilfield Company, SINOPEC, Puyang 457001, China
[3] College of Science, China University of Petroleum, Beijing 102249, China
* Correspondence: xiaomin@cup.edu.cn

Abstract

For condensed-phase detonation, we develop a block-structured adaptive multiresolution method for the reactive compressible Euler equations coupled with the ignition-and-growth model and the JWL (Jones–Wilkins–Lee) equation of state. A second-order Runge–Kutta local time-stepping strategy is employed, and the governing equations are advanced with a two-step operator-splitting procedure. First, the homogeneous conservation laws are discretized by fifth-order WENO (Weighted Essentially Non-Oscillatory) finite differences. Then, the chemical source term is integrated by solving an ordinary differential equation. Because condensed-phase detonations exhibit extremely small characteristic scales in the chemical reaction zone, the proposed method is designed to capture the detonation front, shock waves, and the reaction zone accurately and efficiently. It uses adaptive multiresolution with a reaction zone preservation treatment based on the reaction progress variable to maintain fine resolution in chemically active regions, thereby keeping the lead shock and the reaction zone at the finest grid level. This algorithm significantly improves computational efficiency without compromising key physical features. One-, two-, and three-dimensional benchmark cases are used for validation. The results show that the proposed method accurately captures detonation wave structures and reaction zone characteristics. In particular, compared with uniformly refined computations, it maintains high accuracy while substantially reducing the active-cell count and runtime.

Keywords: condensed-phase detonation; adaptive mesh method; shock front capturing; JWL EOS; adaptive multiresolution

Check for updates

Academic Editors: Junliang Zhao, Huiying Tang and Haibin Chang

Received: 27 May 2026
Revised: 18 June 2026
Accepted: 25 June 2026
Published: 3 July 2026

Copyright: © 2026 by the authors. Licensee MDPI, Basel, Switzerland. This article is an open access article distributed under the terms and conditions of the Creative Commons Attribution (CC BY) license.

1. Introduction

Detonation-driven reactive flows occur widely in engineering applications related to unconventional oil and gas development, such as perforation engineering, explosive fracturing, high-energy gas fracturing, and shock-induced rock breaking. In these scenarios, the inherently flammable and explosive nature of hydrocarbons poses significant safety risks: unintended detonation or deflagration can lead to catastrophic wellbore damage, equipment loss, and environmental hazards. A thorough understanding of detonation-driven reactive flows is therefore essential for both risk mitigation and process optimization. These flows involve strong shock waves, rapid energy release, and multiscale transient structures that govern shock propagation, reaction wave evolution, energy deposition,

and near-wellbore dynamic behavior. Accurate numerical simulation is thus a critical tool for capturing these complex phenomena. However, because the characteristic scales of reaction zones and shock fronts are extremely small compared with the overall computational domain, uniformly refined simulations become prohibitively expensive for practical large-scale applications. Developing efficient and high-fidelity computational acceleration methods for detonation-driven flows is therefore of considerable engineering significance. More broadly, efficient numerical methods for complex reactive and thermal flow problems have attracted increasing attention across a range of engineering disciplines, including regenerative cooling and supercritical-flow heat transfer [1,2].

Condensed-phase detonation is commonly modeled by inviscid reactive flow equations coupled with a reaction law and an equation of state. The ignition-and-growth (IG) model [3] and the Jones–Wilkins–Lee (JWL) equation of state [4] are widely used in detonation and diffraction studies [5–12].

Numerically, the scheme must resolve discontinuities while remaining accurate in smooth regions. ENO/WENO-type methods are standard for this purpose [13–16], and recent variants improve robustness near strong shocks [17–20]. MUSCL (Monotonic Upstream-Centered Schemes for Conservation Laws), approximate Riemann solvers, and PPM (Piecewise Parabolic Method) are also widely used in compressible-flow solvers [21–23], and hybrid strategies continue to be explored for detonation [24]. Still, thin reaction layers often require very fine grids.

Compared with traditional patch-based AMR (Adaptive Mesh Refinement) [25,26], the adaptive multi-resolution method provides an explicit scale decomposition through projection/prediction operators and detail coefficients [27,28]. Therefore, refinement is driven by local multiscale content rather than only by gradient magnitude, and the thresholding process is directly linked to data compression and error control in smooth regions while retaining sharp features near discontinuities. This structure is also naturally compatible with level-dependent local time stepping, so coarse regions are not over-updated when fine regions are constrained by stability or stiffness limits [29–32]. Related work combined block-structured AMR with a rotated lattice Boltzmann flux solver for compressible shock-dominated flows and reported improved efficiency in two- and three-dimensional settings [33].

For reactive flows, recent studies indicate that wavelet criteria are most robust when combined with feature- or physics-based triggers, especially in problems with thin fronts and multi-regime coupling [34–37]. This is directly relevant to condensed-phase detonation. High-resolution diffraction simulations have reported low-pressure/low-density regions, near-corner dead zone behavior, and retonation along the inner wall [6,9]; related dead zone studies also emphasize that physically meaningful front and reaction zone representation requires sustained resolution around the active interface [10]. In addition, multiscale shock-to-detonation analyses for condensed explosives highlight the need for computationally efficient but localized resolution of tightly coupled shock-chemistry processes [8]. Consequently, for the present problem, adaptation should prioritize the lead shock and ignition growth interaction region rather than rely on purely geometric refinement indicators.

In unconventional oil and gas engineering applications, resolving localized shock-reaction structures while maintaining affordable computational cost is particularly important for large-scale simulations involving complex geometries and long propagation distances. In this paper, we present a block-structured adaptive multi-resolution method for condensed-phase detonation. The model uses the reactive Euler equations with the IG model and the JWL EOS. Spatial discretization uses fifth-order WENO finite differences, and temporal integration uses second-order Runge–Kutta local time stepping. The adaptive multi-resolution method follows Harten [27,28], with additional physics-based forced

refinement near the lead shock and reaction zone; the level-dependent time-step design follows established LTS principles [29].

The method is assessed on one-, two-, and three-dimensional benchmarks: strong and weak shock initiation, diffraction around a 90° corner, a two-dimensional center-initiation problem, and a three-dimensional center-initiation problem. The 1D strong-shock and 2D center-initiation cases are used for direct quantitative comparison with uniformly refined solutions; the other cases are used to examine behavior in weak initiation and multidimensional settings. The remainder of this paper is organized as follows. Section 2 introduces the governing equations and reaction rate function. Section 3 introduces the numerical method. Section 4 presents numerical results. Section 5 gives conclusions.

2. Governing Equations

2.1. Compressible Euler Equations

For condensed-phase detonations, the reaction zone thickness is extremely small and the detonation process occurs over a very short time scale. Therefore, heat conduction and viscous effects can be neglected. The governing equations are taken as the compressible Euler equations with chemical reaction source terms, whose form is as follows:

$$\begin{aligned} \frac{\partial \mathbf{U}}{\partial t} + \frac{\partial \mathbf{F}(\mathbf{U})}{\partial x} + \frac{\partial \mathbf{G}(\mathbf{U})}{\partial y} + \frac{\partial \mathbf{H}(\mathbf{U})}{\partial z} &= \mathbf{S}(\mathbf{U}), \\ \mathbf{U} &= \left(\rho, \rho u, \rho v, \rho w, \rho E, \rho \lambda\right)^{\mathrm{T}}, \\ \mathbf{F}(\mathbf{U}) &= \left(\rho u, \rho u^2 + p, \rho uv, \rho uw, (\rho E + p)u, \rho u\lambda\right)^{\mathrm{T}}, \\ \mathbf{G}(\mathbf{U}) &= \left(\rho v, \rho uv, \rho v^2 + p, \rho vw, (\rho E + p)v, \rho v\lambda\right)^{\mathrm{T}}, \\ \mathbf{H}(\mathbf{U}) &= \left(\rho w, \rho uw, \rho vw, \rho w^2 + p, (\rho E + p)w, \rho w\lambda\right)^{\mathrm{T}}, \\ \mathbf{S}(\mathbf{U}) &= \left(0, 0, 0, 0, 0, \rho R\right)^{\mathrm{T}}, \end{aligned} \tag{1}$$

where $\rho, u, v, w, p, E, \lambda$ denote the density, velocity in the x-direction, velocity in the y-direction, velocity in the z-direction, pressure, total energy per unit mass, and mass fraction of products, respectively. The total energy E satisfies the following equation:

$$E = e + \frac{1}{2}(u^2 + v^2 + w^2) + (1 - \lambda)Q, \tag{2}$$

where e represents the internal energy per unit mass, and Q denotes the heat release parameter.

2.2. Equation of State and Reaction Rate

For both condensed-phase explosives and their detonation products, the JWL equation of state is used, which can be expressed in the form of the Mie-Grüneisen equation of state as follows:

$$\begin{aligned} p &= A\exp(-R_1 V) + B\exp(-R_2 V) + \frac{\omega}{V} C_v T, \\ e &= \frac{A}{\rho_0 R_1}\exp(-R_1 V) + \frac{B}{\rho_0 R_2}\exp(-R_2 V) + \frac{C_v T}{\rho_0}, \\ V &= \frac{v}{v_0}, \end{aligned} \tag{3}$$

where v is the specific volume, v_0 is the specific volume at the initial moment, ρ_0, A, B, R_1, R_2, ω are all constants, and T is temperature. For the PBX-9404 and Comp-B explosives, the EOS parameters for the unreacted explosive and the detonation products follow [6,38] and are listed in Table 1 and Table 2, respectively.

Table 1. EOS data for the explosive PBX-9404.

Parameter	Unreacted	Products
A (10^2 GPa)	69.69	8.524
B (10^2 GPa)	−1.727	0.1802
C_v (10^2 GPa/K)	2.505×10^{-5}	1.0×10^{-5}
R_1	7.8	4.6
R_2	3.9	1.3
ω	0.8578	0.38
ρ_0 (g/cm^3)	1.842	1.842

Table 2. EOS data for the explosive Comp-B.

Parameter	Unreacted	Products
A (10^2 GPa)	778.1	5.242
B (10^2 GPa)	−0.05031	0.07678
C_v (10^2 GPa/K)	2.487×10^{-5}	1.0×10^{-5}
R_1	11.3	4.2
R_2	1.13	1.1
ω	0.8938	0.5
ρ_0 (g/cm^3)	1.717	1.717

This paper employs the trinomial ignition growth model as the chemical reaction model, and its specific form is as follows:

$$\begin{aligned} R = {} & I(1-\lambda)^b(\rho/\rho_0 - 1 - a)^x H(\lambda_{\mathrm{IG,max}} - \lambda) \\ & + G_1(1-\lambda)^c \lambda^d p^y H(\lambda_{\mathrm{G_1,max}} - \lambda) \\ & + G_2(1-\lambda)^e \lambda^g p^z H(\lambda_{\mathrm{G_2,min}} - \lambda). \end{aligned} \tag{4}$$

The Lee–Tarver reaction rate parameters for PBX-9404 and Comp-B are listed in Tables 3 and 4.

Table 3. Lee–Tarver reaction rate parameters for PBX-9404.

Parameter	Value	Parameter	Value
I	7.43×10^{11}	b	0.667
a	0.0	x	20.0
G_1	3.1	c	0.667
d	0.111	y	1.0
G_2	400	e	0.333
g	1.0	z	2.0

Table 4. Lee–Tarver reaction rate parameters for Comp-B.

Parameter	Value	Parameter	Value
I	4.0×10^6	b	0.667
a	0.0367	x	7.0
G_1	140	c	0.667
d	0.333	y	2.0
G_2	1000	e	0.222
g	1.0	z	3.0

PBX-9404 is used for the 1D cases and Comp-B for the 2D/3D cases, following the material conventions of the original benchmark studies [6,38]. The same adaptive strategy is applied to both explosives without modification.

3. Numerical Method

3.1. Adaptive Multi-Resolution Method

To resolve fine detonation wave structures efficiently, a block-structured adaptive multi-resolution method is adopted. Fine-grid data are represented by coarse-grid averages together with inter-level differences.

The core of the adaptive multi-resolution method is the multilevel representation of data across different resolution levels. At each level, the numerical solution is stored in the form of cell averages. Two operators are introduced for inter-level data transfer: the projection operator and the prediction operator.

The projection and prediction operators are constructed via the tensor product formulation. In three dimensions, the projection operator is defined as the average over the eight fine-cell children of a coarse cell:

$$P_{l+1\to l}: \quad \bar{u}^{l}_{i,j,k} = \frac{1}{8}\sum_{p=-1}^{0}\sum_{q=-1}^{0}\sum_{r=-1}^{0}\bar{u}^{l+1}_{i+p,j+q,k+r}, \tag{5}$$

where $p, q, r \in \{-1, 0\}$ index the eight children at level $l+1$.

Given the cell averages at level l, the prediction operator reconstructs approximate cell averages for the eight children at level $l+1$:

$$\begin{aligned} P_{l\to l+1}: \quad \hat{u}^{l+1}_{2i+p,2j+q,2k+r} &= \bar{u}^{l}_{i,j,k} + (-1)^{p}T_x + (-1)^{q}T_y + (-1)^{r}T_z \\ &+ (-1)^{(p+1)(q+1)}T_{xy} + (-1)^{(q+1)(r+1)}T_{yz} + (-1)^{(p+1)(r+1)}T_{xz} \\ &- (-1)^{(p+1)(q+1)(r+1)}T_{xyz}, \end{aligned} \tag{6}$$

where the interpolation polynomials T_x, T_y, T_z, T_{xy}, T_{yz}, T_{xz}, and T_{xyz} are constructed from the coefficients α_m $(m = 1, 2)$ as follows:

$$T_x = \sum_{m=1}^{2}\alpha_m\left(\bar{u}^{l}_{i+m,j,k} - \bar{u}^{l}_{i-m,j,k}\right), \tag{7}$$

$$T_y = \sum_{n=1}^{2}\alpha_n\left(\bar{u}^{l}_{i,j+n,k} - \bar{u}^{l}_{i,j-n,k}\right), \tag{8}$$

$$T_z = \sum_{s=1}^{2}\alpha_s\left(\bar{u}^{l}_{i,j,k+s} - \bar{u}^{l}_{i,j,k-s}\right), \tag{9}$$

$$T_{xy} = \sum_{m=1}^{2}\sum_{n=1}^{2}\alpha_m\alpha_n\left(\bar{u}^{l}_{i+m,j+n,k} - \bar{u}^{l}_{i+m,j-n,k} - \bar{u}^{l}_{i-m,j+n,k} + \bar{u}^{l}_{i-m,j-n,k}\right), \tag{10}$$

$$T_{yz} = \sum_{n=1}^{2}\sum_{s=1}^{2}\alpha_n\alpha_s\left(\bar{u}^{l}_{i,j+n,k+s} - \bar{u}^{l}_{i,j+n,k-s} - \bar{u}^{l}_{i,j-n,k+s} + \bar{u}^{l}_{i,j-n,k-s}\right), \tag{11}$$

$$T_{xz} = \sum_{m=1}^{2}\sum_{s=1}^{2}\alpha_m\alpha_s\left(\bar{u}^{l}_{i+m,j,k+s} - \bar{u}^{l}_{i+m,j,k-s} - \bar{u}^{l}_{i-m,j,k+s} + \bar{u}^{l}_{i-m,j,k-s}\right), \tag{12}$$

$$\begin{aligned} T_{xyz} = \sum_{m=1}^{2}\sum_{n=1}^{2}\sum_{s=1}^{2}\alpha_m\alpha_n\alpha_s\big(&\bar{u}^{l}_{i+m,j+n,k+s} - \bar{u}^{l}_{i+m,j+n,k-s} - \bar{u}^{l}_{i+m,j-n,k+s} + \bar{u}^{l}_{i+m,j-n,k-s} \\ &- \bar{u}^{l}_{i-m,j+n,k+s} + \bar{u}^{l}_{i-m,j+n,k-s} + \bar{u}^{l}_{i-m,j-n,k+s} - \bar{u}^{l}_{i-m,j-n,k-s}\big). \end{aligned} \tag{13}$$

In order to obtain fifth-order spatial accuracy, the coefficients are $\alpha_1 = -\frac{22}{128}$, $\alpha_2 = \frac{3}{128}$.

The detail coefficient is defined as the difference between the actual fine-grid value and its predicted value:

$$d_{\mathbf{j}}^{l} = \bar{u}_{\mathbf{j}}^{l} - \hat{u}_{\mathbf{j}}^{l}, \tag{14}$$

where $\mathbf{j}$ denotes the multi-index (i, j, k) in 3D and (i, j) in 2D.

When adjacent blocks reside at different refinement levels, flux consistency across the coarse–fine interface is enforced to preserve conservation. Fine-block fluxes at the interface are averaged to supply the flux for the coarse block, while the coarse-block flux is used to fill ghost cells on the fine-block side at that boundary. For same-level neighbors, ghost cell data are copied directly from the adjacent block's interior. For a block bordering a coarser neighbor, ghost cells are obtained by interpolation from the coarse-block data; for a block bordering a finer neighbor, ghost cell values are computed by averaging the fine-block values that abut the interface. Physical domain boundaries are handled by prescribing the appropriate boundary conditions in the ghost layers before each update stage.

The magnitude of the detail coefficients reflects the local smoothness of the solution at that position and scale. By comparing the detail coefficient with a level-dependent threshold, the mesh can be adaptively refined or coarsened. The threshold is defined as

$$\varepsilon_l = 2^{(l - L_{\max})S} \varepsilon, \tag{15}$$

where $L_{\max}$ is the maximum adaptive refinement level, S is the spatial dimension, and ε is a threshold constant.

In condensed-phase detonation problems, large detail coefficients typically appear near the detonation front and within the chemical reaction zone. The primary refinement driver is the wavelet-based multi-resolution thresholding: blocks with significant detail coefficients are refined, while blocks with sufficiently small coefficients are coarsened.

In addition, a reaction zone preservation treatment based on the reaction progress variable is employed as a supplementary constraint. Cells where $0 < \lambda < 1$ (i.e., the region where chemical reactions are actively taking place) are maintained at the finest grid level to avoid excessive coarsening in chemically active regions and to ensure sufficient resolution for shock–reaction coupling. The lead shock is similarly preserved at the finest level, identified via the pressure or density gradient across the front.

Figure 1 illustrates how the wavelet-based adaptation operates in practice. The black-outlined leaf nodes indicate the cells that are actually advanced in time, while non-leaf nodes only organize the hierarchy. As the detonation front moves to the right, refinement is concentrated around the sharp lead shock and the main reaction zone, whereas smooth upstream and far-product regions remain at coarser levels. This layout illustrates the main objective of the method: to preserve resolution at physically active interfaces while reducing the total number of active cells.

In the present implementation, computational blocks serve as the minimal parallel units, with each block consisting of 16 computational cells. The block-structured multi-resolution framework is parallelized using the Intel Threading Building Blocks (TBB) library. Independent block updates are distributed among TBB tasks, and because data dependencies are mainly localized within neighboring blocks, the block-based organization naturally supports task-level parallel execution with limited communication overhead. Each block is advanced independently through the sequence of homogeneous conservation update, source term integration, and multi-resolution adaptation; inter-block flux consistency and ghost cell exchanges are handled at block boundaries before each stage.

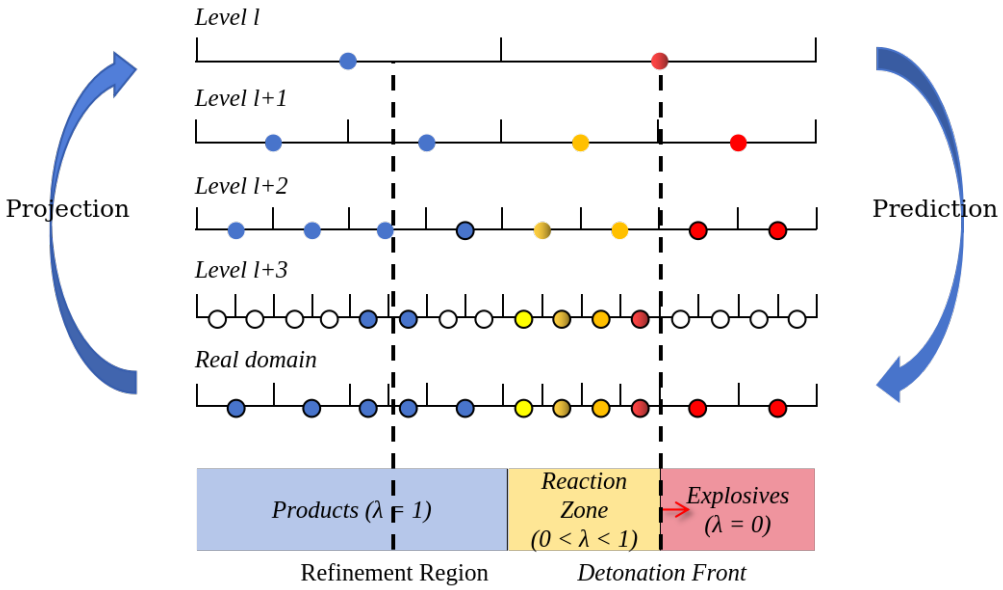


Figure 1. Schematic of the adaptive multi-resolution method for condensed-phase detonation. The arrow indicates the propagation direction of the detonation wave, which moves to the right, with the reaction zone behind it. Circles with black outlines denote leaf nodes, while circles without black outlines denote nodes containing child nodes; filled circles denote valid nodes, and open circles denote empty nodes. The colors distinguish the three regions of the computational domain: product zone (blue, $\lambda = 1$), reaction zone (orange, $0 < \lambda < 1$), and unreacted explosive zone (red, $\lambda = 0$).

3.2. Homogeneous Conservation Update

In this work, the governing equations are solved using a two-step operator-splitting strategy. At each time step, the solution is advanced in two successive stages: first, the homogeneous conservation equations are solved; second, the chemical reaction source term is updated separately.

To capture the reaction zone and wave structures in condensed-phase explosives, the fifth-order WENO-LF (Lax-Friedrichs) finite difference scheme is adopted for spatial discretization.

The semi-discrete form of the homogeneous conservation equations is as follows:

$$\left(\frac{\partial \mathbf{U}}{\partial t}\right)_{i,j,k} = -\frac{\tilde{\mathbf{F}}_{i+\frac{1}{2},j,k} - \tilde{\mathbf{F}}_{i-\frac{1}{2},j,k}}{\Delta x} - \frac{\tilde{\mathbf{G}}_{i,j+\frac{1}{2},k} - \tilde{\mathbf{G}}_{i,j-\frac{1}{2},k}}{\Delta y} - \frac{\tilde{\mathbf{H}}_{i,j,k+\frac{1}{2}} - \tilde{\mathbf{H}}_{i,j,k-\frac{1}{2}}}{\Delta z}. \tag{16}$$

The numerical fluxes are projected onto the local characteristic space for reconstruction, which requires solving the Jacobian matrices $\frac{\partial \mathbf{F}}{\partial \mathbf{U}}$, $\frac{\partial \mathbf{G}}{\partial \mathbf{U}}$ and $\frac{\partial \mathbf{H}}{\partial \mathbf{U}}$ as well as their left and right eigenmatrices. The vector of conserved variables is defined as follows:

$$\mathbf{m} = (m_1, m_2, m_3, m_4, m_5, m_6)^T = (\rho, \rho u, \rho v, \rho w, \rho E, \rho\lambda)^T, \tag{17}$$

and

$$\frac{\partial p}{\partial m_1} = K_1, \quad \frac{\partial p}{\partial m_2} = K_2, \quad \frac{\partial p}{\partial m_3} = K_3, \quad \frac{\partial p}{\partial m_4} = K_4, \quad \frac{\partial p}{\partial m_5} = K_5, \quad \frac{\partial p}{\partial m_6} = K_6. \tag{18}$$

The Jacobian matrix $\mathbf{A} = \frac{\partial \mathbf{F}}{\partial \mathbf{U}}$ is:

$$\mathbf{A} = \begin{bmatrix} 0 & 1 & 0 & 0 & 0 & 0 \\ -u^2 + K_1 & 2u + K_2 & K_3 & K_4 & K_5 & K_6 \\ -uv & v & u & 0 & 0 & 0 \\ -uw & w & 0 & u & 0 & 0 \\ uK_1 - u\left(E + \frac{p}{\rho}\right) & E + \frac{p}{\rho} + uK_2 & uK_3 & uK_4 & u(1+K_5) & uK_6 \\ -u\lambda & \lambda & 0 & 0 & 0 & u \end{bmatrix}. \tag{19}$$

The Jacobian matrix $\mathbf{B} = \frac{\partial \mathbf{G}}{\partial \mathbf{U}}$ is:

$$\mathbf{B} = \begin{bmatrix} 0 & 0 & 1 & 0 & 0 & 0 \\ -uv & v & u & 0 & 0 & 0 \\ -v^2 + K_1 & K_2 & 2v + K_3 & K_4 & K_5 & K_6 \\ -vw & 0 & w & v & 0 & 0 \\ vK_1 - v\left(E + \frac{p}{\rho}\right) & vK_2 & E + \frac{p}{\rho} + vK_3 & vK_4 & v(1+K_5) & vK_6 \\ -v\lambda & 0 & \lambda & 0 & 0 & v \end{bmatrix}. \tag{20}$$

The Jacobian matrix $\mathbf{C} = \frac{\partial \mathbf{H}}{\partial \mathbf{U}}$ is:

$$\mathbf{C} = \begin{bmatrix} 0 & 0 & 0 & 1 & 0 & 0 \\ -uw & w & 0 & u & 0 & 0 \\ -wv & 0 & w & v & 0 & 0 \\ -w^2 + K_1 & K_2 & K_3 & 2w + K_4 & K_5 & K_6 \\ wK_1 - w\left(E + \frac{p}{\rho}\right) & wK_2 & wK_3 & E + \frac{p}{\rho} + wK_4 & w(1+K_5) & wK_6 \\ -w\lambda & 0 & 0 & \lambda & 0 & w \end{bmatrix}. \tag{21}$$

When calculating the left and right eigenmatrices and eigenvalues from the Jacobian matrices, the equation of state is known in the unreacted and detonation product zones, allowing the partial derivatives of pressure with respect to the conserved variables K_1, K_2, K_3, K_4, K_5, and K_6 to be derived directly. However, in the chemical reaction zone where unreacted explosives and detonation products coexist, these partial derivatives cannot be obtained directly. Therefore, this paper assumes that the two constituents move with the same velocity and remain in pressure and temperature equilibrium:

$$\begin{cases} p = p_s = p_g, \\ T = T_s = T_g. \end{cases} \tag{22}$$

Based on this assumption, the internal energy and specific volume of the mixture inside the chemical reaction zone can be obtained through the linear mixing rule:

$$\begin{cases} e = (1-\lambda)e_s + \lambda e_g, \\ v = (1-\lambda)v_s + \lambda v_g, \end{cases} \tag{23}$$

where s and g represent the states of the unreacted explosive and detonation products, respectively. Subsequently, by combining with the equations of state for the unreacted explosive and detonation products, a nonlinear system of equations is constructed and solved to obtain the partial derivatives of pressure with respect to the conserved quantities and the mass fraction of products. The detailed derivation and solution procedure can be found in reference [6].

3.3. Source Term Update

After the homogeneous update, the chemical source term is treated separately for each cell. The semi-discrete form of the source term update is

$$\left(\frac{d\mathbf{U}}{dt}\right)_{i,j} = \tilde{\mathbf{S}}_{i,j}. \tag{24}$$

In the present work, this local ODE is advanced by a second-order TVD Runge–Kutta method. Since the source term does not involve spatial coupling, this step does not affect the conservation property enforced in the hyperbolic update.

3.4. LTS-RK2

The second-order Runge-Kutta local time stepping (LTS-RK2) scheme is used for temporal discretization. To improve the computational efficiency of the adaptive multi-resolution method, Domingues et al. [29] proposed a local time stepping strategy. Instead of enforcing one global time step for all cells, each computational block adopts an adaptive time step: fine-scale blocks use smaller time steps, while coarse-scale blocks use larger time steps. Assuming the time step on the finest level L is Δt, the time step at level l is given by:

$$\Delta t_l = 2^{L-l}\Delta t. \tag{25}$$

This approach satisfies the stability requirement of explicit time discretization and reduces unnecessary updates. Therefore, compared with a single global time step, LTS-RK2 can effectively improve computational efficiency while preserving second-order temporal accuracy in detonation simulations. The update formula is as follows:

$$\begin{aligned} \mathbf{U}^{(1)} &= \mathbf{U}_n + \Delta t \cdot L(\mathbf{U}_n), \\ \mathbf{U}_{n+1} &= \frac{1}{2}\mathbf{U}_n + \frac{1}{2}\left(\mathbf{U}^{(1)} + \Delta t \cdot L(\mathbf{U}^{(1)})\right), \end{aligned} \tag{26}$$

where $L(\mathbf{U})$ is the spatial discretization operator (including flux terms and source terms), and Δt is the local time step determined by the CFL (Courant-Friedrichs-Lewy) condition.

The level-based LTS strategy of Domingues et al. is adopted here because it is naturally integrated within the adaptive multi-resolution hierarchy and has been extensively validated for wavelet-based adaptive methods [29,30]. Alternative approaches such as multi-rate time integration may offer additional flexibility in handling multiple temporal scales; a systematic comparison of different local-integration strategies is left for future work.

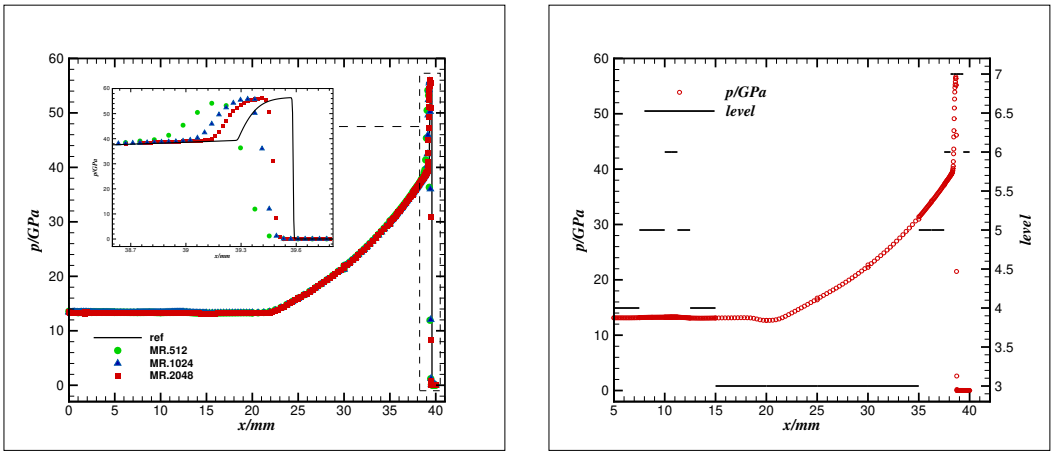
4. Numerical Results

4.1. 1D Strong Shock Initiation

The computational domain is set to 40 mm, with PBX-9404 selected as an example. A sustained incident pressure is imposed as the boundary condition to investigate the shock initiation process. In the present simulation, the incident pressure is fixed at 16 GPa.

Figure 2 compares solutions from the adaptive multi-resolution method at different maximum resolutions with a reference uniform-grid solution. The reference solution is computed on a uniform grid with 10,000 cells using a CFL number of 0.01 and fifth-order WENO-LF reconstruction. As the maximum resolution increases, the profiles from the adaptive multi-resolution method move toward the reference solution. In Figure 2b, the refinement-level distribution shows that the highest levels are concentrated near the lead shock and the main reaction region, while smooth regions remain at coarser levels, which is consistent with the localized resolution strategy of the adaptive multi-resolution method.

Figures 3 and 4 further illustrate the two main evolution stages of strong-shock initiation. In Stage 1 (Figure 3), the incident shock compresses the explosive and triggers early reaction, generating a pressure pulse. Under sustained incident pressure loading, this pulse is continuously amplified and progressively approaches the lead shock, where their coupling strengthens the shock intensity. In Stage 2 (Figure 4), the sustained incident pressure further promotes amplification of the pressure pulse and its coupling with the chemical reaction zone, eventually leading to complete reaction and formation of a stable detonation wave.



(**a**) Pressure distributions.

(**b**) Pressure distributions with different resolutions.

Figure 2. This figure contains two subfigures. (**a**) Pressure profile comparison: blue circles, green triangles, and red squares denote numerical results with maximum resolutions of 512, 1024, and 2048, respectively; the black solid line denotes the reference solution. (**b**) Pressure distributions and adaptive multi-resolution refinement-level distribution at a maximum computational level of 7.

In addition, tracer points are placed along the propagation direction at uniform intervals of 3.2 mm to record the temporal evolution of key physical quantities, including pressure and product mass fraction. The corresponding histories are shown in Figure 5. The pressure histories exhibit successive abrupt rises associated with the arrival of the lead shock, and the response at downstream tracer points is progressively delayed in time as the wave propagates through the explosive. The histories of the product mass fraction show a short induction interval following shock compression, after which λ increases rapidly toward the fully reacted state. These results indicate that, under strong shock loading, chemical reactions are triggered shortly after shock passage and the coupling between the lead shock and the reaction zone remains strong throughout the initiation process.

The data compression ratio is defined as

$$\eta_{\text{Data}} = \frac{N_{\text{NonMR}} - N_{\text{MR}}}{N_{\text{NonMR}}}, \tag{27}$$

where N_{NonMR} denotes the total number of cells in the uniformly refined grid and N_{MR} denotes the maximum number of active cells in the adaptive multi-resolution method. The computational time compression ratio is defined as

$$\eta_{\text{Time}} = \frac{T_{\text{NonMR}} - T_{\text{MR}}}{T_{\text{NonMR}}}, \tag{28}$$

where T_{NonMR} and T_{MR} represent the total computational times of the uniform-grid and multi-resolution simulations, respectively. Table 5 summarizes the comparisons of computational cost and data storage between the two approaches under different maximum resolutions.

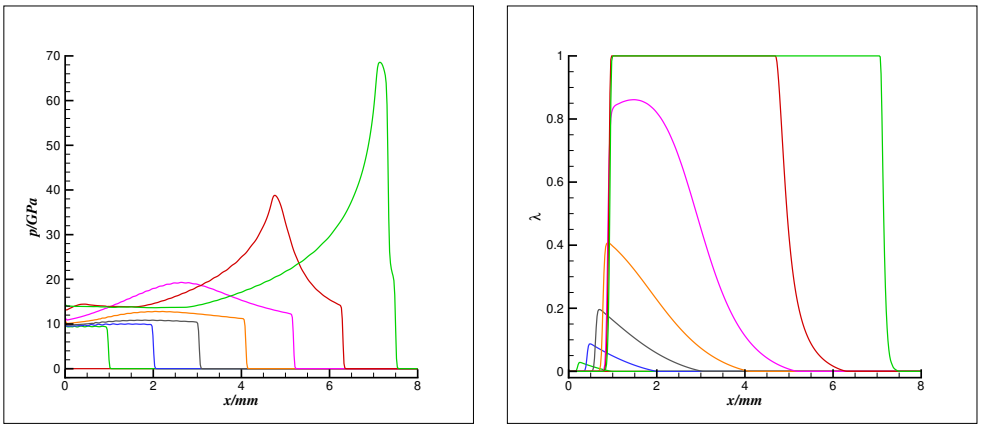


Figure 3. Stage 1: pressure p (**left**) and reaction progress variable λ (**right**) distributions at $t = 0$ µs to 0.35 µs with a time interval of 0.05 µs. Different colored curves denote successive temporal snapshots within this time interval.

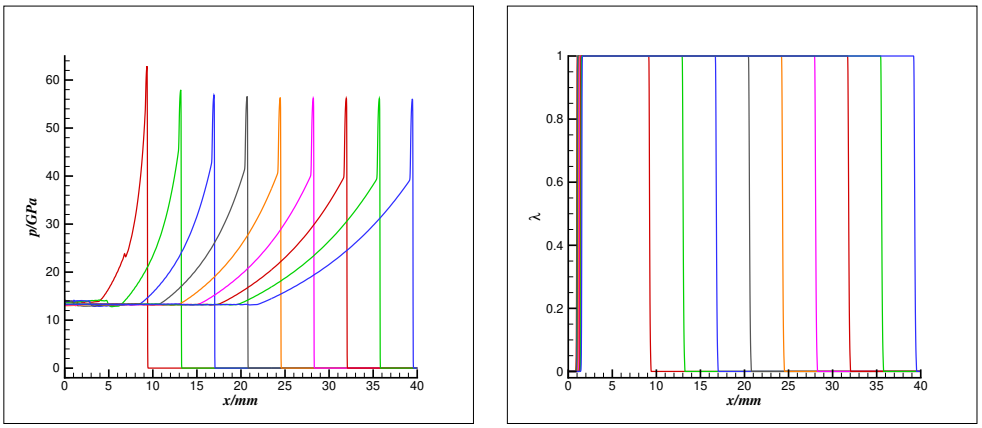


Figure 4. Stage 2: pressure p (**left**) and reaction progress variable λ (**right**) distributions at $t = 0.4$ µs to 1.2 µs with a time interval of 0.1 µs. Different colored curves denote successive temporal snapshots within this time interval.

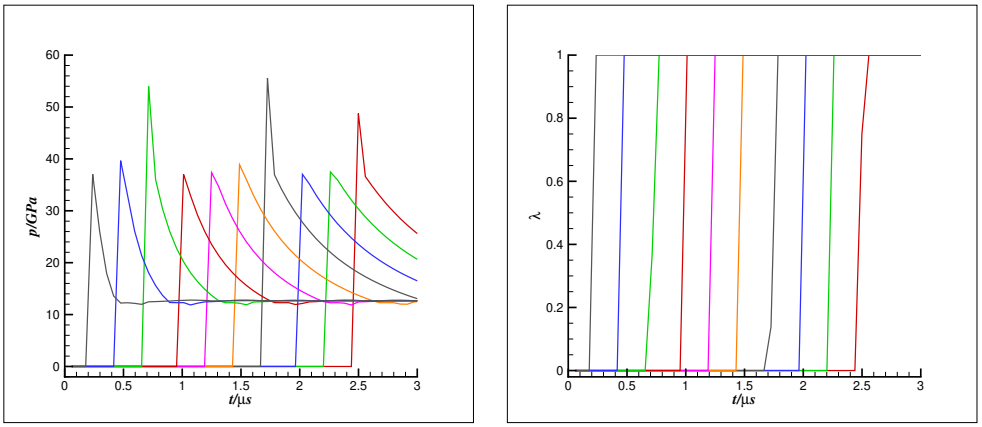


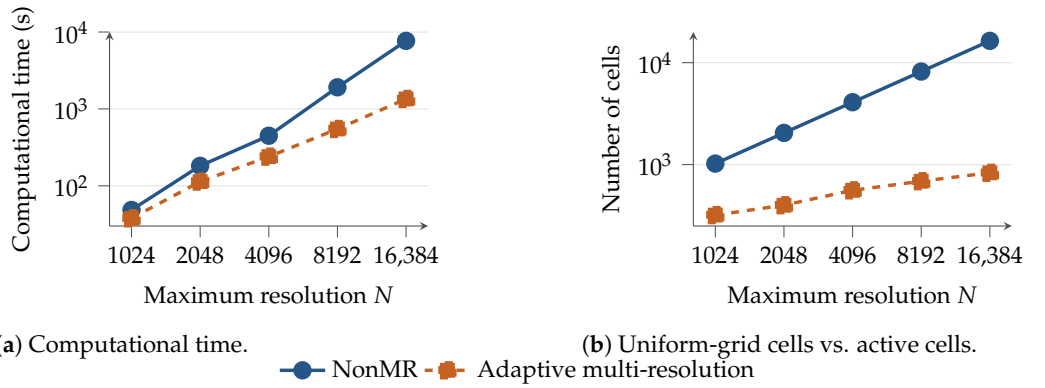
Figure 5. Tracer point histories of pressure p (**left**) and reaction progress variable λ (**right**) for the 1D strong shock initiation case. Different colored curves denote histories recorded at different tracer-point locations along the propagation direction.

As shown in Table 5 and Figure 6, the computation with the adaptive multi-resolution method remains consistently less expensive than the corresponding NonMR computation in both runtime and cell count. As the maximum resolution increases from 1024 to 16,384, the NonMR computational time grows from 48.55 s to 7678.12 s, whereas the computational

time of the adaptive multi-resolution method grows from 37.82 s to only 1346.82 s. A similar highlight is observed in the number of cells: the uniform-grid cell count increases directly with N, while the maximum number of active cells in the adaptive multi-resolution method increases only from 320 to 832. This direct comparison shows that, for the strong-shock benchmark considered in this work, the proposed method can substantially reduce the number of computational cells while maintaining accuracy, so the relative advantage of the adaptive multi-resolution method becomes more pronounced as the reference uniform grid is refined.

Table 5. Comparison of computational cost and data storage between the uniform-grid and the adaptive multi-resolution method.

N	1024	2048	4096	8192	16,384
T_{NonMR} (s)	48.55	181.89	448.01	1911.00	7678.12
T_{MR} (s)	37.82	113.47	239.47	548.56	1346.82
η_{Time}	22.10%	37.62%	46.55%	71.29%	82.46%
N_{NonMR}	1024	2048	4096	8192	16384
N_{MR}	320	400	560	688	832
η_{Data}	68.75%	80.47%	86.33%	91.60%	94.92%



(**a**) Computational time. (**b**) Uniform-grid cells vs. active cells.

Figure 6. Direct comparison between the uniform-grid (NonMR) and the adaptive multi-resolution computations for the 1D strong-shock initiation benchmark. Both vertical axes are logarithmic.

In this benchmark, the adaptive multi-resolution method consistently concentrates the finest resolution on the dynamically dominant region around the lead shock and the main reaction zone, which is the key reason for the observed cost reduction.

4.2. 1D Weak Shock Initiation

To examine mildly driven initiation, a weak shock case is considered. The computational domain and material properties remain identical to those of the strong shock case, while a reduced sustained incident pressure is imposed at the boundary to generate a slower initiation process characterized by an extended induction zone.

In this benchmark, the incident pressure is set to 1.5 GPa, corresponding to a relatively weak incident shock strength. Although the incident pressure is low, the sustained loading eventually drives the explosive past the initiation threshold, leading to a gradual buildup of chemical reactions prior to the formation of a self-sustained detonation.

Figures 7–9 illustrate the evolution of the pressure and reaction progress variable distributions during the weak shock initiation process, which can be divided into three distinct stages. Figure 7 corresponds to the initial induction stage ($t = 0$ µs to 0.3 µs), where the incident shock propagates into the explosive. At this stage, the chemical reaction is initiated but remains weak, and the pressure behind the shock front is relatively low. This early post-shock sharp feature can be interpreted as a weak reaction-induced pressure

pulse formed behind the lead shock: under weak loading, ignition has started but heat release is still limited, so the pulse remains only loosely coupled to the front during the induction stage and has not yet evolved into a fully developed detonation structure. In other words, the lead shock and the main heat-release zone are still partially separated in this period, which explains the long induction interval observed in the weak-shock case. Figure 8 shows the reaction growth stage ($t = 0.3$ μs to 2.0 μs). As the reaction progresses, energy release leads to a pressure buildup behind the leading shock, causing the reaction zone to accelerate and the shock strength to increase. Compared with Stage 1, this stage is characterized by progressive shock–reaction recoupling: the pressure pulse is amplified, and the distance between the active reaction region and the leading shock gradually decreases. Figure 9 depicts the transition to detonation ($t = 2.0$ μs to 2.3 μs). In this final stage, the reaction wave catches up with the shock front, resulting in a rapid pressure spike and the formation of a self-sustained detonation wave. The solution from the adaptive multi-resolution method resolves the full transition, from a long induction period to rapid shock–reaction coupling during detonation formation. Overall, the three-stage sequence indicates a clear weak-initiation pathway: delayed ignition, gradual amplification, and final runaway coupling to a self-sustained front. This case shows that the method preserves the full weak-initiation pathway without global refinement during the mostly smooth early evolution.

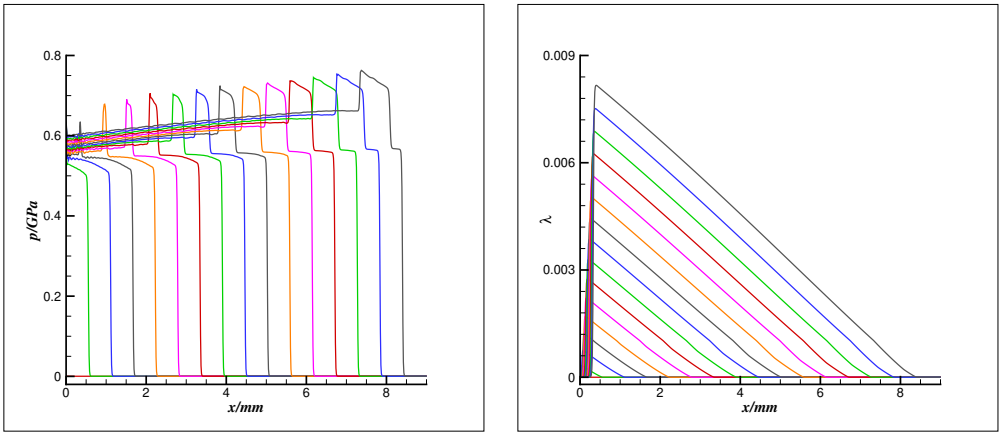


Figure 7. Stage 1: pressure p (**left**) and reaction progress variable λ (**right**) distributions at $t = 0$ μs to 0.3 μs. Different colored curves denote successive temporal snapshots within this time interval.

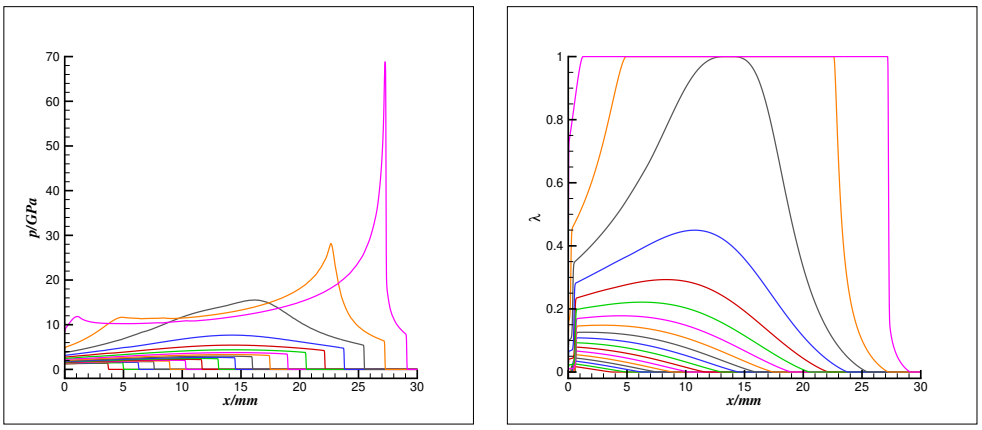


Figure 8. Stage 2: pressure p (**left**) and reaction progress variable λ (**right**) distributions at $t = 0.3$ μs to 2.0 μs. Different colored curves denote successive temporal snapshots within this time interval.

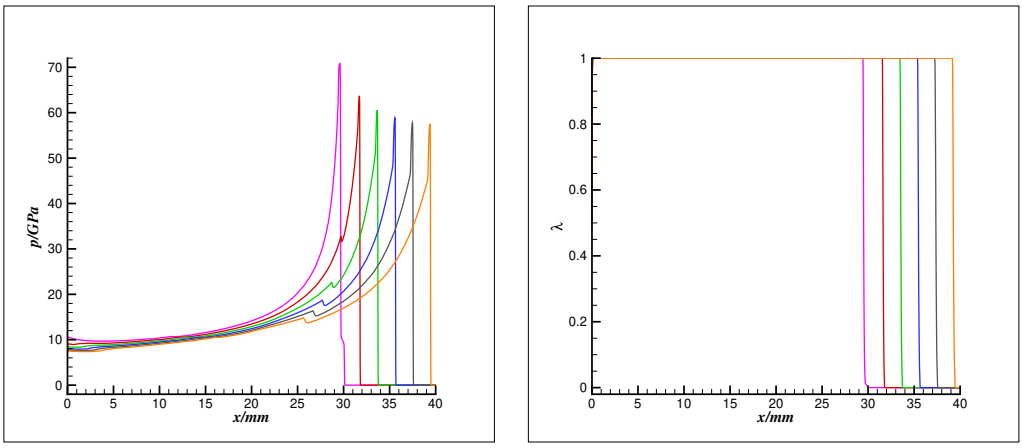


Figure 9. Stage 3: pressure p (**left**) and reaction progress variable λ (**right**) distributions at $t = 2.0$ µs to 2.3 µs. Different colored curves denote successive temporal snapshots within this time interval.

4.3. 2D Planar Detonation Diffraction Around a 90° Corner

The diffraction of a planar detonation wave around a sharp corner represents a classical benchmark problem because it includes shock reflection, rarefaction, and reaction zone distortion in one configuration. In this study, a two-dimensional computational domain $(0, 15\ \text{mm}) \times (0, 15\ \text{mm})$ containing a 90° corner geometry is considered, with the corner vertex located at $(x, y) = (5\ \text{mm}, 7.5\ \text{mm})$, in which a planar detonation wave propagates toward the corner and subsequently diffracts into the transverse channel.

For the two-dimensional benchmarks, Comp-B is selected as the explosive material, and the same reactive Euler framework is used together with the corresponding JWL equation of state and ignition-and-growth reaction model for Comp-B; the EOS parameters are listed in Table 2, and the reaction rate parameters are listed in Table 4, following [38]. At the initial time, a CJ detonation front is initialized at $x = 1$ mm and propagates toward the corner. The left boundary is prescribed as an inflow boundary, the right boundary is prescribed as an outflow boundary, and the upper and lower boundaries are prescribed as solid walls. Before the detonation front reaches the corner at $t = 0.5$ µs, the wave gradually develops into a stable detonation structure. The finest resolution used in this case is 1536×1536.

Figure 10 presents density, pressure, and reaction progress variable contours at selected time instants obtained by the adaptive multi-resolution method. Figure 11 shows the pressure and product mass fraction distributions within 3 mm along the inner wall at $t = 0.8$ µs, 1.0 µs, 1.2 µs, and 1.4 µs. The contours show that when the detonation front reaches the corner, sudden lateral expansion generates a strong rarefaction wave, which temporarily weakens the wave and reduces pressure near the inner wall. As a result, ignition is delayed in the explosive near the wall, and the reaction zone broadens. The profiles along the inner wall provide a consistent temporal signature: an early pressure drop and delayed increase in λ, followed by pressure recovery and renewed product formation as transverse shock structures develop. As the front continues to propagate downward along the inner wall, this reignition process produces a retonation wave and drives further reaction in previously unreacted material. At $t = 1.4$ µs, material within about 1 mm of the inner wall remains unreacted, whereas material farther from the wall is nearly fully reacted, indicating a localized dead zone near the corner.

The adaptive multi-resolution method resolves the sharp gradients at the lead shock, reaction zone, and transverse structures, and reproduces the front curvature and post-diffraction wave pattern. Overall, the contour fields and inner-wall profiles consistently capture the sequence of near-corner weakening, delayed reaction, and subsequent reigni-

tion. This benchmark serves as a qualitative validation of the method's ability to resolve complex unsteady wave structures, rather than a quantitative comparison with reference data.

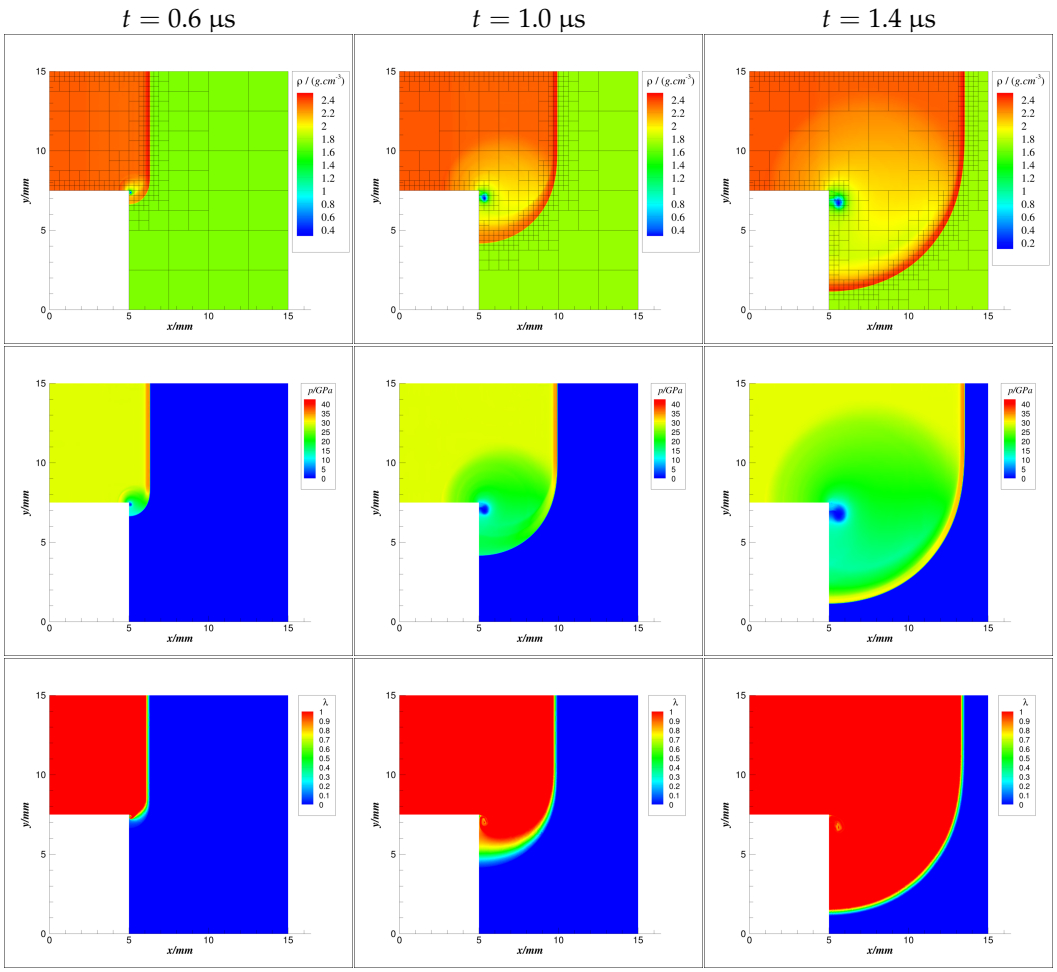


Figure 10. Density (with multi-resolution block structure), pressure, and reaction progress variable distributions from top to bottom at $t = 0.6$ μs, 1.0 μs, and 1.4 μs from left to right, respectively, for the corner diffraction problem.

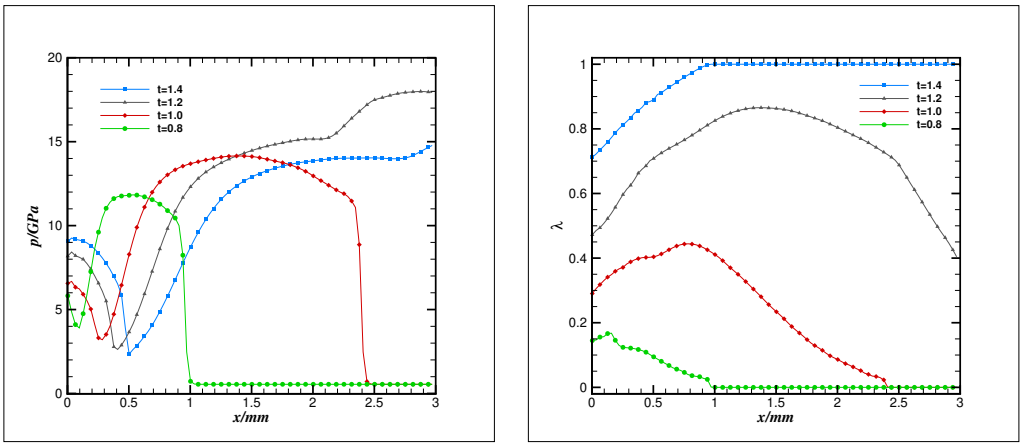


Figure 11. Pressure p (**left**) and reaction progress variable λ (**right**) distributions along the inner wall at 3 mm for $t = 0.8$ μs to 1.4 μs.

4.4. 2D Center Initiation Problem

To examine multidimensional detonation dynamics with expanding curved fronts, a two-dimensional center-initiation problem is considered. Reactions are triggered at the center of the computational domain, and an expanding circular detonation wave then propagates into the surrounding explosive.

The computational domain is initialized with quiescent Comp-B explosive material at ambient conditions on $(0, 10\ \text{mm}) \times (0, 10\ \text{mm})$. All four boundaries are treated as solid-wall boundary conditions. A circular region centered at $(5\ \text{mm}, 5\ \text{mm})$ with radius 0.04 mm is initialized with the CJ state to trigger detonation. This initialization launches a stable expanding detonation wave from the domain center. The finest resolution used in this case is 2048×2048.

Figure 12 illustrates the density, pressure, and reaction progress variable contours at $t = 0.6\ \mu\text{s}$, $0.8\ \mu\text{s}$, and $1.0\ \mu\text{s}$. Following ignition, a strong shock is generated and rapidly coupled with the chemical energy release, forming an expanding circular detonation front. The reaction zone remains tightly attached to the lead shock as the detonation propagates outward from the center. The contour fields also exhibit strong geometric symmetry with respect to the center $(5\ \text{mm}, 5\ \text{mm})$: the pressure and reaction progress distributions remain centro-symmetric as the front expands. This indicates that the adaptive strategy preserves symmetry well throughout front expansion rather than introducing visible distortion.

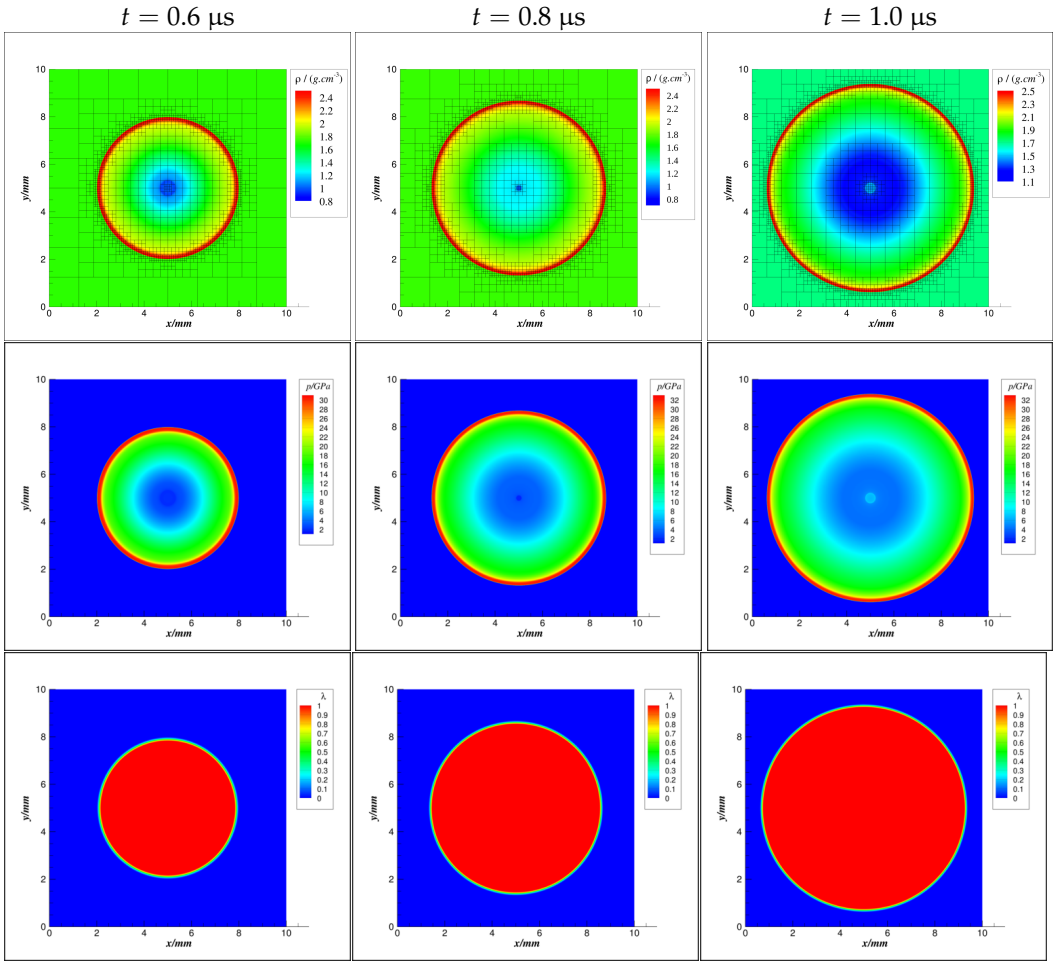


Figure 12. Density (with multi-resolution block structure), pressure, and reaction progress variable distributions from top to bottom at $t = 0.6\ \mu\text{s}$, $0.8\ \mu\text{s}$, and $1.0\ \mu\text{s}$ from left to right, respectively.

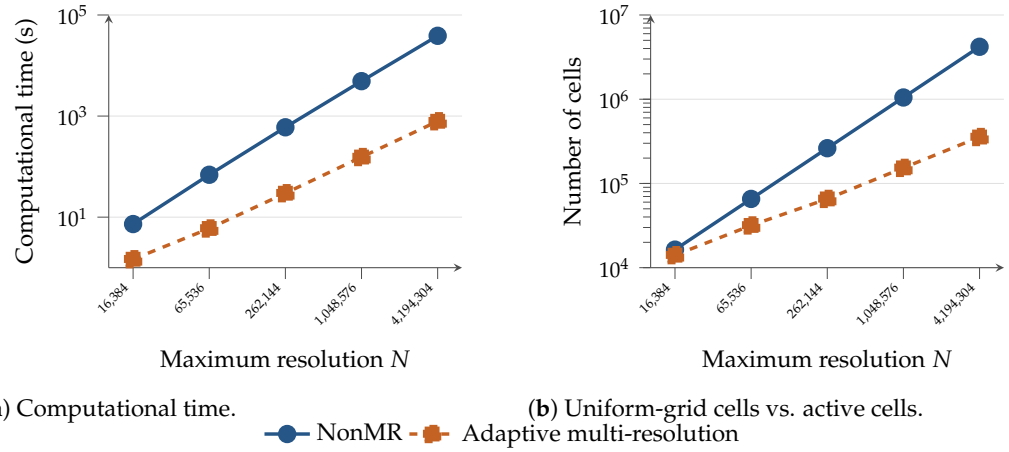
These results support adaptive multi-resolution as an effective high-fidelity alternative to uniform refinement for detonation problems with strongly localized structures. Future

work will extend the present framework to more complex reaction models and broader engineering geometries.

Table 6 reports the quantitative compression metrics for this case, including runtime, active cell count, and their corresponding reduction ratios. Figure 13 gives the same comparison in graphical form. The time and cell count curves both show a widening separation between the adaptive and uniform-grid computations as N increases, which is consistent with the increasing values of η_{Time} and η_{Data} in the table. Together with the contour evolution in Figure 12, these data show that as the curved front expands, the block-structured adaptive mesh follows the physically active perimeter while limiting growth of active cells in the smooth interior.

Table 6. Compression metrics for the 2D center-initiation case at different uniform-grid resolutions.

N	16,384	65,536	262,144	1,048,576	4,194,304
T_{NonMR} (s)	7.30	68.98	599.84	4906.91	38,754.3
T_{MR} (s)	1.47	5.97	29.76	154.64	789.41
η_{Time}	79.86%	91.35%	95.04%	96.85%	97.96%
N_{NonMR}	16,384	65,536	262,144	1,048,576	4,194,304
N_{MR}	14,080	31,744	65,536	153,088	355,840
η_{Data}	14.06%	51.56%	75.00%	85.40%	91.52%



(**a**) Computational time. (**b**) Uniform-grid cells vs. active cells.

Figure 13. Direct comparison between the uniform-grid (NonMR) and adaptive multi-resolution computations for the 2D center-initiation benchmark. The x-axis tick labels are rotated and comma-separated to improve readability. Both vertical axes are logarithmic.

4.5. 3D Center Initiation Problem

To assess three-dimensional performance, a center-initiation case is simulated in a cubic domain $(0, 10\text{ mm}) \times (0, 10\text{ mm}) \times (0, 10\text{ mm})$. The material is initially quiescent Comp-B at ambient conditions, and a small spherical region centered at $(5\text{ mm}, 5\text{ mm}, 5\text{ mm})$ with radius 0.04 mm is initialized at the CJ state to trigger detonation. All six boundaries are treated as solid walls. The finest resolution used in this case is $512 \times 512 \times 512$.

After ignition, a strong spherical shock forms and quickly couples with the chemical energy release, producing an expanding, nearly spherical detonation front. As shown in Figure 14, the density field exhibits a thin, spherical high-density shell that marks the leading shock, and the pressure field shows a corresponding region of elevated pressure concentrated near the propagating front. The reaction progress variable λ shows the post-shock chemical evolution in the region behind the leading shock. The overlaid multi-resolution block structure in all three panels further demonstrates that refinement remains localized around this steep-gradient shell, while smoother regions are kept comparatively

coarse. Figure 15 further presents the time evolution using contour maps on the mid-plane slice $z = 5$ mm at $t = 0.4$ µs, 0.8 µs, and 1.2 µs.

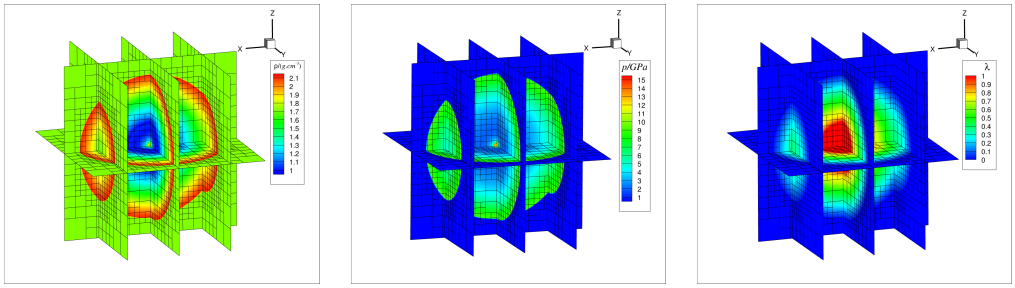


Figure 14. Three-dimensional center-initiation results at $t = 1.2$ µs. From left to right: density ρ, pressure p, and reaction progress variable λ shown on the three orthogonal mid-plane slices ($x = 5$ mm, $y = 5$ mm, and $z = 5$ mm), with the multi-resolution block structure overlaid in each panel. The adaptive multi-resolution method concentrates refinement near the expanding spherical detonation front.

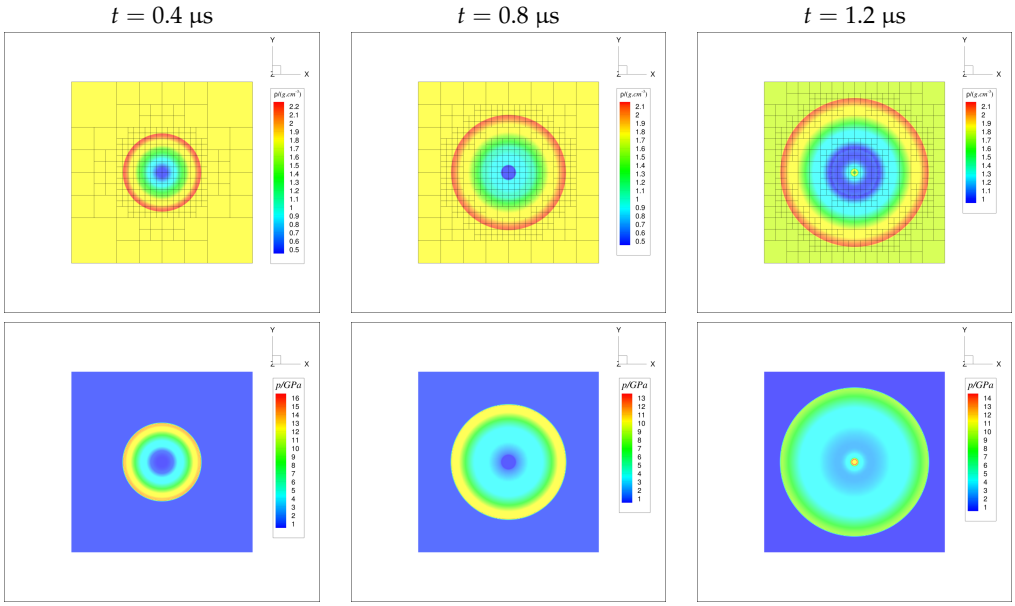


Figure 15. $z = 5$ mm slice contour maps for the three-dimensional center-initiation case. **Top row**: density ρ; **bottom row**: pressure p. Columns correspond to $t = 0.4$ µs, 0.8 µs, and 1.2 µs (**left** to **right**). The overlapping "Z" label does not affect the scientific interpretation of the contour fields.

These results indicate that the method maintains a stable, self-sustained spherical detonation front in three dimensions while preserving efficiency by restricting the finest resolution to the shock–reaction region.

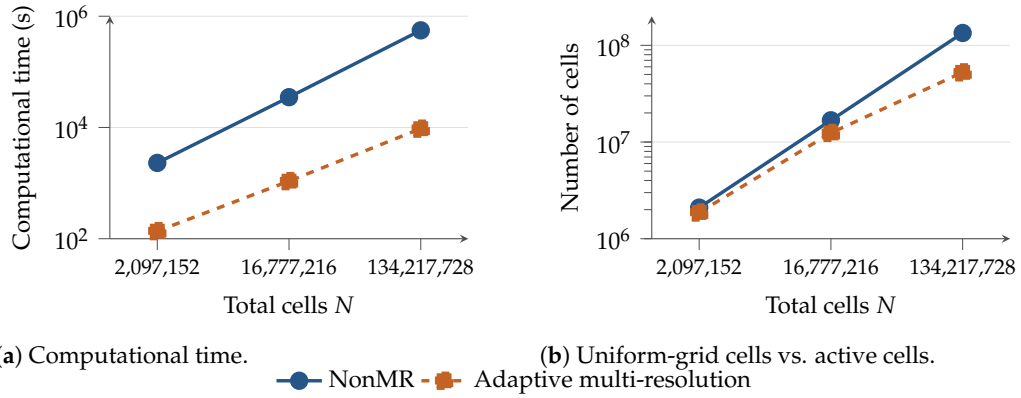
To quantify the computational advantage in three dimensions, Table 7 summarizes the runtime, active-cell count, and corresponding compression ratios for the 3D center-initiation case at three equivalent uniform-grid resolutions. The MR computations use a $16 \times 16 \times 16$ base block with 3, 4, and 5 refinement levels, corresponding to equivalent uniform grids of 128^3, 256^3, and 512^3, respectively.

As shown in Table 7 and Figure 16, the adaptive multi-resolution method achieves substantial reductions in both runtime and active-cell count in three dimensions. At the finest resolution (N = 134,217,728), the time compression ratio reaches 98.29% and the data compression ratio reaches 60.84%. The separation between the adaptive and uniform curves widens as the resolution increases, indicating that the relative efficiency gain grows with problem size. These 3D trends are consistent with the 1D and 2D results, confirming

that the method scales favorably to three-dimensional simulations where the expanding spherical detonation front remains a localized steep-gradient structure within a much larger smooth domain.

Table 7. Comparison of computational cost and data storage between the uniform-grid and the adaptive multi-resolution method for the 3D center-initiation case.

N	2,097,152	16,777,216	134,217,728
T_{NonMR} (s)	2305.98	35,059.40	557,444.46
T_{MR} (s)	136.90	1085.52	9516.36
η_{Time}	94.06%	96.90%	98.29%
N_{NonMR}	2,097,152	16,777,216	134,217,728
N_{MR}	1,867,776	12,419,072	52,559,872
η_{Data}	10.94%	25.98%	60.84%



(**a**) Computational time. (**b**) Uniform-grid cells vs. active cells.

Figure 16. Direct comparison between the uniform-grid (NonMR) and adaptive multi-resolution computations for the 3D center-initiation benchmark. Both vertical axes are logarithmic.

5. Conclusions

In this paper, a block-structured adaptive multi-resolution method has been developed for detonation in condensed-phase explosives. Because the operator-splitting framework decouples the hydrodynamic solver from the thermodynamic closure, the adaptive multi-resolution core can be extended to alternative equations of state—such as the stiffened-gas EOS and the Clausius-Clapeyron (CC) EOS—without structural modification. However, the thermodynamic closure and the associated numerical flux evaluation must be adapted to the specific EOS being employed, as the pressure, sound speed, and characteristic wave structures depend on the thermodynamic model. The proposed method employs a wavelet-coefficient threshold criterion as the primary refinement driver, supplemented by a reaction zone preservation treatment ($0 < \lambda < 1$) that maintains fine resolution in chemically active regions and at the lead shock, ensuring that the lead shock and the chemical reaction zone remain at the finest grid level throughout the computation, while reducing computational cost and maintaining the accuracy.

The method couples fifth-order WENO spatial discretization with an operator-splitting technique and level-dependent local time stepping. In one-dimensional strong-shock initiation, comparisons with a uniform-grid reference indicate that the adaptive solution approaches the reference trend as resolution increases; runtime and cell count metrics also confirm clear efficiency gains. In the 2D center-initiation problem, comparisons with the uniform-grid computation likewise show fewer active cells and shorter runtime. The weak-shock and two-dimensional benchmarks further demonstrate that the method captures long induction behavior, curved fronts, and post-diffraction wave interactions in more complex flow fields. In the 3D center-initiation case, the method successfully tracks the

expanding spherical detonation front with a time compression ratio exceeding 98% at the finest resolution.

These results show that adaptive multi-resolution is an efficient alternative to uniform refinement when key fluid flow structures are localized. Future work will extend the method to richer reaction models and more complex geometries.

Author Contributions: Conceptualization, M.X.; methodology, S.J., Y.W., G.Q. and S.P.; software, S.J., Q.Y. and J.Z.; validation, S.J. and W.J.; writing—original draft preparation, S.J.; writing—review and editing, Y.W. and M.X. All authors have read and agreed to the published version of the manuscript.

Funding: This work is supported by the Foundation of the State Key Laboratory of Petroleum Resources and Engineering, China University of Petroleum, Beijing (Grant No. PRE/DX-2507), the National Natural Science Foundation of China (Grant No. 12102052) and the Science Foundation of China University of Petroleum, Beijing (Grant No. 2462023YJRC008).

Data Availability Statement: The data presented in this study are openly available on GitHub at [https://github.com/713626/mr_for_detonation] (accessed on 24 June 2026).

Conflicts of Interest: Author Shuxia Jiang, Guixue Qi, Song Peng, Qikui Yu, Jixi Zhang, and Wencai Jiang were employed by the SINOPEC Key Laboratory of Development Technology of Sour Natural Gas Fields and Zhongyuan Oilfield Company, SINOPEC. The remaining authors declare that the research was conducted in the absence of any commercial or financial relationships that could be construed as a potential conflict of interest.

References

1. Liu, J.; Guo, W.; Yin, M.; Sunden, B. Flow and heat transfer characteristic of regenerative cooling channels using supercritical CO_2 with circular tetrahedral lattice structures. *Case Stud. Therm. Eng.* **2025**, *71*, 106204. [CrossRef]
2. Liu, J.; Guo, W.; Zhao, G.; Ma, J.; Xi, W.; Sunden, B. Study on heat transfer characteristics of supercritical CO_2/*n*-decane composite double triangular regenerative cooling for scramjets. *Aerosp. Sci. Technol.* **2026**, *172*, 111725.
3. Lee, E.L.; Tarver, C.M. Phenomenological model of shock initiation in solid explosives. *Phys. Fluids* **1980**, *23*, 2362–2372. [CrossRef]
4. Lee, E.L.; Hornig, H.C.; Kury, J.W. *Adiabatic Expansion of High Explosive Detonation Products*; Tech. Rep. UCRL-50422; Lawrence Radiation Laboratory: Livermore, CA, USA, 1968.
5. Kapila, A.K.; Schwendeman, D.W.; Bdzil, J.B.; Henshaw, W.D. A study of detonation diffraction in the ignition-and-growth model. *Combust. Theory Model.* **2007**, *11*, 781–822. [CrossRef]
6. Wang, C.; Liu, X. High resolution numerical simulation of detonation diffraction of condensed explosives. *Int. J. Comput. Methods* **2015**, *12*, 1550005. [CrossRef]
7. Yu, J.; Zhang, X.; Chen, J.; Xu, Y. A high-order simulation method for compressible multiphase flows with condensed-phase explosive detonation in underwater explosions. *Phys. Fluids* **2024**, *36*, 016104. [CrossRef]
8. Lee, S.; Fahrenthold, E.P. Multiscale simulation of shock to detonation in condensed phase explosives. *J. Appl. Phys.* **2022**, *132*, 175905. [CrossRef]
9. Ma, T.; Ma, F.; Li, P.; Li, J. High-resolution numerical simulation of detonation diffraction. *Sci. Sin. Technol.* **2021**, *51*, 281–292. [CrossRef]
10. Ma, T.; Ma, F.; Ning, J. High-resolution numerical simulation of detonation propagation and dead zones in LX-17. *Propellants Explos. Pyrotech.* **2020**, *45*, 1705–1713. [CrossRef]
11. Sen, O.; Rai, N.K.; Diggs, A.S.; Hardin, D.B.; Udaykumar, H.S. Multi-scale shock-to-detonation simulation of pressed energetic material: A meso-informed ignition and growth model. *J. Appl. Phys.* **2018**, *124*, 085110. [CrossRef]
12. Tropin, D.A.; Lavruk, S.A. Numerical simulation of the interaction of heterogeneous detonation with an inhomogeneous porous insert. *Int. J. Multiph. Flow* **2023**, *162*, 104407. [CrossRef]
13. Jiang, G.S.; Shu, C.W. Efficient implementation of weighted ENO schemes. *J. Comput. Phys.* **1996**, *126*, 202–228. [CrossRef]
14. Harten, A.; Engquist, B.; Osher, S.; Chakravarthy, S.R. Uniformly high order accurate essentially non-oscillatory schemes, III. *J. Comput. Phys.* **1987**, *71*, 231–303. [CrossRef]
15. Liu, X.-D.; Osher, S.; Chan, T. Weighted essentially non-oscillatory schemes. *J. Comput. Phys.* **1994**, *115*, 200–212. [CrossRef]
16. Shu, C.-W.; Osher, S. Efficient implementation of essentially non-oscillatory shock-capturing schemes. *J. Comput. Phys.* **1988**, *77*, 439–471. [CrossRef]
17. Fan, C.; Zhang, X.; Qiu, J. Positivity-preserving high order finite difference WENO schemes for compressible Navier–Stokes equations. *J. Comput. Phys.* **2022**, *467*, 111446. [CrossRef]

18. Fan, C.; Zhang, X.; Qiu, J. Positivity-preserving high order finite volume hybrid Hermite WENO schemes for compressible Navier–Stokes equations. *J. Comput. Phys.* **2021**, *445*, 110596. [CrossRef]
19. Li, Q.; Yokoi, K.; Xie, Z.; Omar, S.; Xue, J. A fifth-order high-resolution shock-capturing scheme based on modified weighted essentially non-oscillatory method and boundary variation diminishing framework for compressible flows and compressible two-phase flows. *Phys. Fluids* **2021**, *33*, 056104. [CrossRef]
20. Liang, T.; Fu, L. A new high-order shock-capturing TENO scheme combined with skew-symmetric-splitting method for compressible gas dynamics and turbulence simulation. *Comput. Phys. Commun.* **2024**, *302*, 109236. [CrossRef]
21. Colella, P.; Woodward, P.R. The piecewise parabolic method (PPM) for gas-dynamical simulations. *J. Comput. Phys.* **1984**, *54*, 174–201. [CrossRef]
22. Roe, P.L. Approximate Riemann solvers, parameter vectors, and difference schemes. *J. Comput. Phys.* **1981**, *43*, 357–372. [CrossRef]
23. van Leer, B. Towards the ultimate conservative difference scheme. V. A second-order sequel to Godunov's method. *J. Comput. Phys.* **1979**, *32*, 101–136. [CrossRef]
24. Bouguellab, N.; Khalfallah, S.; Zebiri, B.; Brahmi, N. Hybrid conservative central/WENO finite difference scheme for two-dimensional detonation problems. *Int. J. Comput. Methods Eng. Sci. Mech.* **2023**, *25*, 10–29. [CrossRef]
25. Berger, M.J.; Oliger, J. Adaptive mesh refinement for hyperbolic partial differential equations. *J. Comput. Phys.* **1984**, *53*, 484–512. [CrossRef]
26. Berger, M.J.; Colella, P. Local adaptive mesh refinement for shock hydrodynamics. *J. Comput. Phys.* **1989**, *82*, 64–84. [CrossRef]
27. Harten, A. Adaptive multiresolution schemes for shock computations. *J. Comput. Phys.* **1994**, *115*, 319–338. [CrossRef]
28. Harten, A. Multiresolution algorithms for the numerical solution of hyperbolic conservation laws. *Commun. Pure Appl. Math.* **1995**, *48*, 1305–1342. [CrossRef]
29. Domingues, M.O.; Gomes, S.M.; Roussel, O.; Schneider, K. An adaptive multiresolution scheme with local time stepping for evolutionary PDEs. *J. Comput. Phys.* **2008**, *227*, 3758–3780. [CrossRef]
30. Lopes, M.M.; Domingues, M.O.; Schneider, K.; Mendes, O. Local time-stepping for adaptive multiresolution using natural extension of Runge–Kutta methods. *J. Comput. Phys.* **2019**, *382*, 291–318. [CrossRef]
31. Kaiser, J.W.J.; Hoppe, N.; Adami, S.; Adams, N.A. An adaptive local time-stepping scheme for multiresolution simulations of hyperbolic conservation laws. *J. Comput. Phys. X* **2019**, *4*, 100038. [CrossRef]
32. Sreejith, N.A.; Riber, E.; Cuenot, B. Analysis and design of a local time stepping scheme for LES acceleration in reactive and non-reactive flow simulations. *J. Comput. Phys.* **2022**, *470*, 111580. [CrossRef]
33. Huang, X.; Chen, J.; Zhang, J.; Wang, L.; Wang, Y. An adaptive mesh refinement–rotated lattice Boltzmann flux solver for numerical simulation of two and three-dimensional compressible flows with complex shock structures. *Symmetry* **2023**, *15*, 1909. [CrossRef]
34. Peng, H.; Deiterding, R. High-resolution numerical simulation of rotating detonation waves with parallel adaptive mesh refinement. *Appl. Energy Combust. Sci.* **2025**, *21*, 100316. [CrossRef]
35. Gusto, B.; Plewa, T. A hybrid adaptive multiresolution approach for the efficient simulation of reactive flows. *Comput. Phys. Commun.* **2022**, *274*, 108300. [CrossRef]
36. Stock, A.; Moureau, V. Feature-based adaptive mesh refinement for multi-regime reactive flows. *Proc. Combust. Inst.* **2024**, *40*, 105488. [CrossRef]
37. Ma, W.; Luo, D.; Ying, W.; Ni, G.; Xiao, M.; Chen, Y. Adaptive multi-resolution method for 3D reactive flows with level set front capturing. *Commun. Comput. Phys.* **2023**, *33*, 849–883. [CrossRef]
38. Urtiew, P.A.; Vandersall, K.S.; Tarver, C.M.; Garcia, F.; Forbes, J.W. *Shock Initiation Experiments and Modeling of Composition B and C-4*; Tech. Rep. UCRL-CONF-222137; Lawrence Livermore National Laboratory: Livermore, CA, USA, 2006.

Disclaimer/Publisher's Note: The statements, opinions and data contained in all publications are solely those of the individual author(s) and contributor(s) and not of MDPI and/or the editor(s). MDPI and/or the editor(s) disclaim responsibility for any injury to people or property resulting from any ideas, methods, instructions or products referred to in the content.